



Fabrication of C/X-TiO₂@C₃N₄ NTs (X=N, F, Cl) composites by using phenolic organic pollutants as raw materials and their visible-light photocatalytic performance in different photocatalytic systems

Kexin Li^{a,b,1}, Zhenxing Zeng^{b,1}, Liushui Yan^b, Mingxin Huo^{a,*}, Yihang Guo^a, Shenglian Luo^{b,*}, Xubiao Luo^b

^a Jilin Engineering Research Centre for Municipal Wastewater Treatment and Water Quality Protection, School of Environment, Northeast Normal University, ChangChun 130117, People's Republic of China

^b Key Laboratory of Jiangxi Province for Persistent Pollutants Control and Resources Recycle, NanChang Hangkong University, NanChang 330063, People's Republic of China



ARTICLE INFO

Article history:

Received 13 November 2015

Received in revised form 14 January 2016

Accepted 19 January 2016

Available online 22 January 2016

Keywords:

Heterojunction

Carbon nitride nanotubes

Co-doped titanium dioxide

Degradation

Hydrogen evolution

ABSTRACT

A series of nonmetallic elements co-doped titanium dioxide coated carbon nitride nanotubes (C/X-TiO₂@C₃N₄ NTs, X=N, F, Cl) was successfully prepared by a simple sol-gel-pyrolysis process using phenolic organic pollutants, titanium butoxide, and carbon nitride nanotubes as precursors. The morphology, porosity, phase and chemical structure, and optical and electronic property of as-prepared C/X-TiO₂@C₃N₄ NTs were well characterized. The as-prepared C/X-TiO₂@C₃N₄ NTs exhibited excellent visible-light photocatalytic activity in the conventional degradation and hydrogen evolution systems compared with traditional TiO₂/g-C₃N₄ heterojunction, which is attributed to their unique tubular nanostructure and nonmetallic elements co-doped TiO₂ component. Subsequently, the visible-light photocatalytic activity of C/X-TiO₂@C₃N₄ NTs was further studied in the simultaneous hydrogen evolution with organic pollutant degradation system on the basis of our previous work. The reaction mechanisms in different photocatalytic systems were further discussed in detail.

© 2016 Elsevier B.V. All rights reserved.

1. Introduction

The arbitrary emission of organic phenolic wastewater caused many environmental problems with the development of industry and agriculture [1–6]. The treatment and recycling of organic phenolic wastewater is a severe challenge for every environmental scientist. Photocatalytic oxidation technique by using visible-light response photocatalyst is an economical and effective way toward organic phenolic wastewater treatment [7–10]. In recent years, the photocatalytic degradation of aqueous phenolic organic pollutants has been widely studied [11–13]. However, there are few reports with regard to the recycling of aqueous phenolic organic pollutants.

Titanium dioxide (TiO₂) and graphitic carbon nitride (g-C₃N₄) are two representative semiconductor photocatalysts and have

been extensively studied because of their advantages such as low cost, environmentally friendly, and unique band gap structure [14–19]. Recent studies show that constructing heterostructure between TiO₂ and g-C₃N₄ is an effective strategy to improve the visible-light-induced charge separation efficiency owing to the electron transfer from the conduction band (CB) of g-C₃N₄ to that of TiO₂ [20–25]. However, the band gap structure drawbacks of TiO₂ and the morphology disadvantages of g-C₃N₄ severely limit the visible-light activity of TiO₂/g-C₃N₄ heterojunction. On the one hand, the wide band gap leads to the lack of visible-light response of TiO₂ [26]. On the other hand, bulk layered structure of g-C₃N₄ with low specific surface area cause the photogenerated electron hard to transfer to the catalyst surface [27,28]. Nonmetallic elements co-doping and nanostructure design are the effective strategies to solve the defects of TiO₂ and g-C₃N₄ [29–34]. For example, Chen et al. developed C-, N-, and S-doped TiO₂ nanomaterials to achieve the visible-light response of TiO₂; Yang et al. fabricated g-C₃N₄ nanosheets using a liquid-exfoliation method to enhance the visible-light photocatalytic activity of bulk layered g-C₃N₄; Huang et al. present a facile synthesis method to produce a ternary

* Corresponding authors.

E-mail addresses: huomx097@nenu.edu.cn (M. Huo), sllou@hnu.edu.cn (S. Luo).

¹ These two authors contributed equally to this work.

structure of BCN (boron carbon nitride) nanosheets that has a functionality to catalyse hydrogen and oxygen evolution from water as well as CO_2 reduction under visible light illumination [35–37]. Our previous studies also show that graphene doping can bring about the visible-light response of TiO_2 and constructing tubular nanostructure can effectively improve the visible-light activity of bulk layered g- C_3N_4 [38–40].

In this article, for fabricating a new type $\text{TiO}_2/\text{g-}\text{C}_3\text{N}_4$ heterojunction with excellent visible-light photocatalytic activity, a series of $\text{C}/\text{X-}\text{TiO}_2@\text{C}_3\text{N}_4$ NTs ($\text{X}=\text{N, F, Cl}$) composites were successfully prepared by a simple sol-gel-pyrolysis method using phenolic organic pollutants (phenol, *p*-nitrophenol, *p*-fluorophenol, and *p*-chlorophenol), titanium butoxide, and carbon nitride nanotubes as precursors. The co-doped nonmetallic elements and constructed tubular nanostructure solve the shortcomings of TiO_2 and g- C_3N_4 component in the conventional $\text{TiO}_2/\text{g-}\text{C}_3\text{N}_4$ system. Therefore, the visible-light photocatalytic activity of as-prepared $\text{C}/\text{X-}\text{TiO}_2@\text{C}_3\text{N}_4$ NTs is significantly higher than that of conventional $\text{TiO}_2/\text{g-}\text{C}_3\text{N}_4$ heterojunction.

The photocatalytic performance of as-prepared $\text{C}/\text{X-}\text{TiO}_2@\text{C}_3\text{N}_4$ NTs was preliminarily evaluated in conventional degradation and hydrogen evolution systems under $\lambda > 420\text{ nm}$ visible-light irradiation using methyl orange and *p*-chlorophenol as target pollutants and triethylamine as an electron donor. Both organic pollutant degradation and hydrogen evolution photocatalytic reactions are based on the same photo-induced charge transfer process. However, the above photocatalytic reactions are performed usually by different photocatalysts under different experimental conditions because of the difference in their required charge transfer characteristics [41]. Specifically, organic pollutant degradation reaction is attributed to the single-electron transfer under aerobic conditions whereas hydrogen evolution reaction is carried out by two-electron transfer in the absence of oxygen. Our previous studies show that some organic pollutants, such as *p*-chlorophenol and rhodamine B, of which redox potential is more negative than the valence band (VB) potential of the photocatalyst can be used as an electron donor for photocatalytic hydrogen evolution reaction [42]. The degradation of organic pollutant only relies on the oxidation of photogenerated holes in the simultaneous hydrogen evolution with organic pollutant degradation photocatalytic system. In this article, the impact of organic pollutant concentration and photocatalytic reaction time on the hydrogen yield and degradation efficiency in the simultaneous hydrogen evolution with organic pollutant degradation photocatalytic system will be further studied, and the reaction mechanisms in different photocatalytic systems will be further discussed in detail.

2. Experimental

2.1. Chemicals and reagents

Melamine ($\text{C}_3\text{H}_6\text{N}_6$, AR grade) was purchased from Tianjin Damao Chemical Reagent. Titanium butoxide ($\text{Ti}(\text{OC}_4\text{H}_9)_4$, $\geq 99.0\%$, abbreviated TBT), phenol ($\text{C}_6\text{H}_6\text{O}$, GC grade), *p*-nitrophenol ($\text{C}_6\text{H}_5\text{NO}_3$, GC grade, abbreviated PNP), *p*-fluorophenol ($\text{C}_6\text{H}_5\text{OF}$, 99%, abbreviated PFP), *p*-chlorophenol ($\text{C}_6\text{H}_5\text{OCl}$, GC grade, abbreviated PCP) were purchased from Aladdin Chemistry Co. Ltd. Triethylamine ($(\text{C}_2\text{H}_5)_3\text{N}$, AR grade, abbreviated TEA) was purchased from Shanghai Fine Chemical Technology Co. Ltd. Methyl orange ($\text{C}_{14}\text{H}_{14}\text{N}_3\text{NaO}_3\text{S}$, AR grade, abbreviated MO) and rhodamine B ($\text{C}_{28}\text{H}_{31}\text{ClN}_2\text{O}_3$, AR grade, abbreviated RB) were purchased from Shanghai Fine Chemical Technology Co. Ltd. All chemicals were used without further purification. Double distilled water was used in the catalyst preparation and subsequent catalytic tests.

2.2. Preparation

2.2.1. Preparation of carbon nitride nanotubes (C₃N₄ NTs) by one-step hydrothermal treatment strategy

Pure g- C_3N_4 was prepared by directly calcining melamine in air. Typically, 50 g of melamine powder was put into a 100 mL alumina crucible with a cover. The crucible was heated to 250 °C from room temperature in a muffle furnace at a heating rate of 5 °C/min, and then continued heated to 550 °C at a heating rate of 10 °C/min. Keeping the temperature at 550 °C for 2 h, yellow g- C_3N_4 was obtained after natural cooling. C₃N₄ NTs was fabricated according to our previous work by one-step hydrothermal treatment strategy with g- C_3N_4 as precursor [39]. First, 1 g of g- C_3N_4 powder was uniformly dispersed into 30 mL HCl (2 mol L⁻¹) using a 500 W ultrasonic cracher for 1 h. After stirring the resulting suspension for 1 h at room temperature, the suspension was subject to hydrothermal treatment at 150 °C for 24 h at a heat rate of 1 °C/min. The final C₃N₄ NTs were obtained by drying at 60 °C for 24 h and thermal treatment at 120 °C for 24 h, respectively. For comparison, C₃N₄ NTs (400 °C) sample was also prepared by calcining the obtained C₃N₄ NTs at 400 °C for 2 h.

2.2.2. Preparation of C/X-TiO₂@C₃N₄ NTs (X=N, F, Cl) composites by a simple sol-gel-pyrolysis process

In a typical synthesis, 1 g of C₃N₄ NTs was uniformly dispersed into 10 mL EtOH using a 500 W ultrasonic cracher for 10 min. 7.1×10^{-4} mol phenolic organic pollutant (phenol: 66.7 mg, PNP: 98.7 mg, PFP: 79.5 mg, or PCP: 91.3 mg) was dissolved into 5.0 mL EtOH and 3.0 mL H₂O, and a TBT/EtOH/HOAc solution was prepared by pouring 2.5 mL TBT into 5.0 mL EtOH and 0.25 mL HOAc with vigorous stirring for 5 min. Subsequently, the above TBT/EtOH/HOAc and phenolic organic pollutant/EtOH/H₂O solution were successively added drop wise to the C₃N₄ NTs/EtOH solution to form a translucent yellow sol, and the stirring was continued until the hydrogel was formed. The obtained hydrogel was slowly dehydrated at room temperature, 45 °C, and 60 °C for 12 h, respectively. The final products were obtained after calcining the xerogel at 400 °C for 2 h, and denoted as C-TiO₂@C₃N₄ NTs for phenol doping or C/X-TiO₂@C₃N₄ NTs for PNP, PFP, and PCP doping, where X represents the doped N, F, or Cl element in the products. For comparison, TiO₂, C-TiO₂, C/X-TiO₂, TiO₂@g-C₃N₄, and TiO₂@C₃N₄ NTs samples were also prepared by the same experimental procedure.

2.3. Characterizations

Field emission scanning electron microscopy (FESEM) images were recorded using a Nova NanoSEM450 field emission scanning electron microscope. The chemical compositions and elemental mappings of the samples were determined by energy-dispersive X-ray spectrometer (EDX) equipped on FESEM. Transmission electron microscopy (TEM) images were recorded on a JEOL JEM-2010 transmission electron microscope at an accelerating voltage of 200 kV. Nitrogen gas porosimetry measurements were performed on a Quantachrome NOVA 2000e surface area and porosity analyzer after the samples were outgassed under a vacuum at 70 °C for 20 min and 150 °C for 6 h. X-ray diffraction (XRD) patterns were obtained using a Panalytical X'Pert PRO diffractometer via Cu K α radiation. Fourier transform infrared (FTIR) spectra were recorded on a Bruker VERTEX 70 FTIR apparatus. X-ray photoelectron spectra (XPS) was performed using a VG-ADES 400 instrument with an Mg K α -ADES source at a residual gas pressure of less than 10^{-8} Pa. UV-vis/diffuse reflectance spectroscopy (UV-vis/DRS) was conducted using a Lambda 750S UV/VIS/NIR spectrometer. The Mott-Schottky plot to evaluate the flat-band potential (V_{fb}) of the semiconductor space charge region was obtained by measuring impedance spectra at fixed frequency of 1000 Hz. A conventional

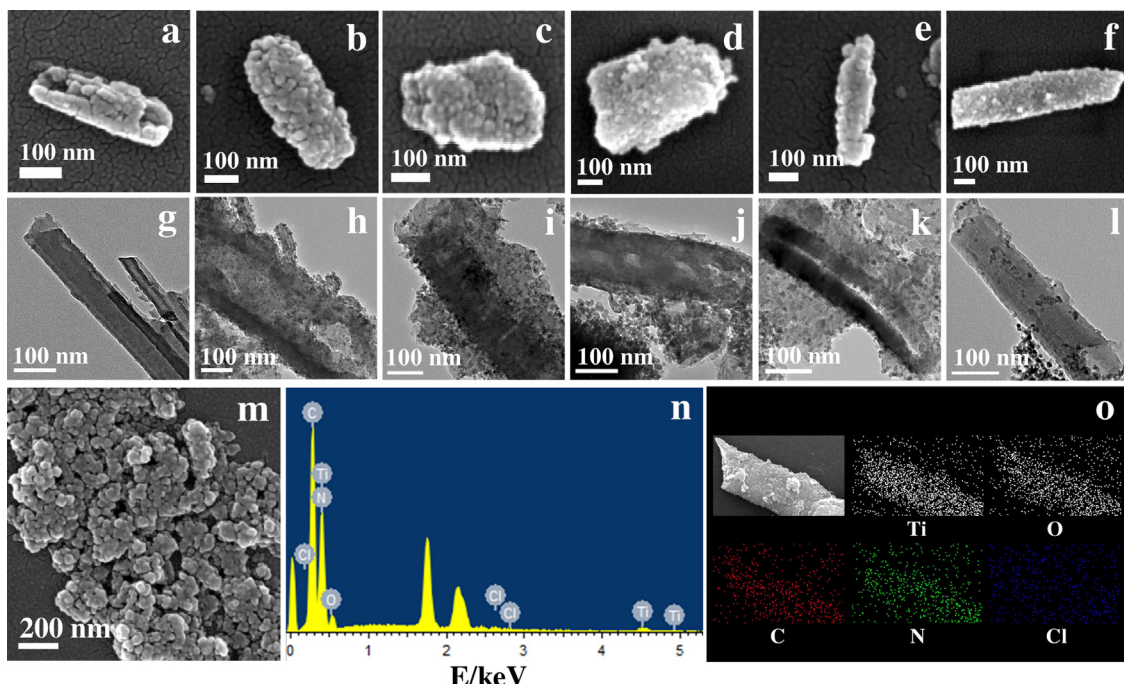


Fig. 1. FESEM images of C_3N_4 NTs (a), $\text{TiO}_2@\text{C}_3\text{N}_4$ NTs (b), $\text{C-TiO}_2@\text{C}_3\text{N}_4$ NTs (c), $\text{C/N-TiO}_2@\text{C}_3\text{N}_4$ NTs (d), $\text{C/F-TiO}_2@\text{C}_3\text{N}_4$ NTs (e), $\text{C/Cl-TiO}_2@\text{C}_3\text{N}_4$ NTs (f), and TiO_2 (m); TEM images of C_3N_4 NTs (g), $\text{TiO}_2@\text{C}_3\text{N}_4$ NTs (h), $\text{C-TiO}_2@\text{C}_3\text{N}_4$ NTs (i), $\text{C/N-TiO}_2@\text{C}_3\text{N}_4$ NTs (j), $\text{C/F-TiO}_2@\text{C}_3\text{N}_4$ NTs (k), and $\text{C/Cl-TiO}_2@\text{C}_3\text{N}_4$ NTs (l); EDX spectrum (n) and elemental mappings (o) of $\text{C/Cl-TiO}_2@\text{C}_3\text{N}_4$ NTs.

three electrode cells using a BioLogic VSP electrochemical workstation (Claix, France) was used to determine the V_{fb} of the sample. The catalyst sample was deposited on a $1\text{ cm} \times 2\text{ cm}$ FTO conducting glass served as working electrode, while the SCE as the reference electrode and Pt as the counter electrode. Photoluminescence (PL) measurements were carried out on a HITACHI F-7000 fluorescence spectrophotometer.

2.4. Photocatalytic tests

2.4.1. Photocatalytic degradation of aqueous MO and PCP

A PLS-SXE300 Xe lamp (300W, Beijing PerfectLight Co. Ltd., China) served as the light source, and the output wavelength $\lambda > 320\text{ nm}$. The visible-light irradiation was obtained by removing the UV irradiation from the lamp using a 420 nm cut filter, which can control the output wavelength $\lambda > 420\text{ nm}$. 100 mg of solid photocatalyst and 100 mL of organic pollutant (MO or PCP) aqueous solution were poured into a 300 mL self-designed quartz reactor. The initial concentrations of MO and PCP are 10 mg L^{-1} and 20 mg L^{-1} , respectively. The suspension was ultrasonicated for 10 min and stirred in the dark until adsorption-desorption equilibrium. Subsequently, the light source was switched on, and further stirring was applied. The temperature of the suspension was maintained at $35 \pm 2^\circ\text{C}$ by circulation of water through an external cooling jacket. At specific intervals of irradiation, fixed amounts of the reaction solution were extracted, centrifuged, and filtered. Changes in the MO concentrations were analyzed using an UNICO UV-2000 spectrophotometer at $\lambda = 464$. Changes in the PCP concentrations were analyzed using an Agilent 1100 series high-performance liquid chromatography (HPLC): C_{18} column, UV detector ($\lambda = 277\text{ nm}$), and acetonitrile/water (60/40 v/v) was used as a mobile phase at a flow rate of 1.0 mL/min . Changes of total organic carbon (TOC) in the reaction system were monitored using a Shimadzu TOC-L CSH total organic carbon analysis system.

2.4.2. Hydrogen evolution from water-splitting by using TEA as an electron donor

100 mg of solid photocatalyst loaded with 3 wt% of Pt co-catalyst and 100 mL of H_2O containing 20 vol% TEA were poured into a 300 mL quartz reactor. The above suspension was ultrasonicated for 10 min and stirred in dark for 1 h. Subsequently, the light source was switched on, and further stirring was applied. The temperature of the suspension was maintained at $35 \pm 2^\circ\text{C}$ by circulation of water through an external cooling jacket. After $\lambda > 420\text{ nm}$ visible-light irradiation for 6 h, the generated hydrogen was *in situ* analyzed with a GC 7890-II TCD gas chromatograph (TECHCOMP) using an MS-5 A column, which was connected to the gas circulating line with argon carrier.

2.4.3. Simultaneous hydrogen evolution with organic pollutant degradation

The initial hydrogen evolution system, that is 100 mL of H_2O containing 20 vol% TEA, was replaced by 100 mL of organic pollutant aqueous solution. The initial concentration of organic pollutant (PCP or RB) aqueous solution is 20 mg L^{-1} . The adsorption-desorption equilibrium between organic pollutant and photocatalyst need to be reached before the start of hydrogen evolution reaction, and the saturated photocatalyst was separated and putted into a new reaction solution. $\text{C/N-TiO}_2@\text{C}_3\text{N}_4$ NTs was selected as a tested photocatalyst and the irradiation time is 6 h. For comparison, the photocatalytic tests were also performed in pure H_2O system, pure TEA system, and RB/ H_2O system with different RB concentrations or reaction time. The generated hydrogen was *in situ* analyzed with a GC 7890-II TCD gas chromatograph. Change in the PCP concentration was analyzed using an Agilent 1100 series HPLC. Change in the RB concentration was analyzed using an UNICO UV-2000 spectrophotometer at $\lambda = 554\text{ nm}$.

3. Results and discussion

3.1. Characterizations

3.1.1. Morphology and textural property

The morphology of as-prepared materials was characterized by FESEM and TEM observations (Fig. 1). As shown in Fig. 1a and m, C_3N_4 NTs exhibits an open end and hollowed tubular nanostructure, moreover, pure TiO_2 exhibits a microstructure of nanoparticles aggregation. Our previous work has demonstrated that the tubular nanostructure was fabricated by the condensation of surface $-\text{OH}$ of $\text{g-C}_3\text{N}_4$ nanosheets via a nanosheets roll-up mechanism [39]. Specifically, the $\text{g-C}_3\text{N}_4$ nanosheets were obtained by peeling off bulk $\text{g-C}_3\text{N}_4$ in acidic conditions using an ultrasonic crusher, and then the unbonded surface $-\text{NH}_2$ groups of $\text{g-C}_3\text{N}_4$ nanosheets were substituted with $-\text{OH}$ groups in the course of hydrothermal reaction under acidic conditions. As a result, the C_3N_4 NTs were constructed by the condensation of surface $-\text{OH}$ on the $\text{g-C}_3\text{N}_4$ nanosheets. For the $\text{TiO}_2@\text{C}_3\text{N}_4$ NTs, $\text{C-TiO}_2@\text{C}_3\text{N}_4$ NTs, and $\text{C/X-TiO}_2@\text{C}_3\text{N}_4$ NTs samples, the FESEM results shown in Fig. 1b–f prove that TiO_2 nanoparticles were successfully coated on the surface of C_3N_4 NTs. The diameter of an individual nanotube depends on the diameter of an individual C_3N_4 NTs and the cover thickness of TiO_2 nanoparticles. The EDX spectrum and elemental mappings of $\text{C/Cl-TiO}_2@\text{C}_3\text{N}_4$ NTs prove the existence of Ti, O, C, N, and Cl elements in the composite (Fig. 1n and o). The TEM results of as-prepared materials are consistent with the above FESEM results. For the TEM image of C_3N_4 NTs shown in Fig. 1g, the outer diameters of these two C_3N_4 NTs are approximately 80 and 40 nm, respectively, and the wall thicknesses of these two C_3N_4 NTs are approximately 20 and 10 nm, respectively. This result indicates that the size and wall thickness of an individual C_3N_4 NTs can not be controlled and determined by the size and thickness of a curly $\text{g-C}_3\text{N}_4$ nanosheets unit. The TEM images of $\text{TiO}_2@\text{C}_3\text{N}_4$ NTs, $\text{C-TiO}_2@\text{C}_3\text{N}_4$ NTs, and $\text{C/X-TiO}_2@\text{C}_3\text{N}_4$ NTs samples shown in Fig. 2h–l further indicate that TiO_2 nanoparticles were successfully coated on the surface of C_3N_4 NTs.

The textural property of as-prepared materials was characterized by nitrogen gas porosity measurement (Fig. 2). As shown in Fig. 2a, the type II isotherm of $\text{g-C}_3\text{N}_4$ indicates its non-porous characteristic of bulk layered structure and the type IV isotherm with H3-type hysteresis loop for the C_3N_4 NTs and C_3N_4 NTs (400 °C) samples indicate that the mesoporous structures are constructed by the accumulation of nanotubes structural units. The type IV isotherms with H4-type hysteresis loops for the TiO_2 , $\text{TiO}_2@\text{C}_3\text{N}_4$ NTs, $\text{C-TiO}_2@\text{C}_3\text{N}_4$ NTs, and $\text{C/X-TiO}_2@\text{C}_3\text{N}_4$ NTs samples are originated from their tiny slit-type mesoporous structures, which are constructed by the close accumulation of TiO_2 nanoparticles. As shown in Fig. 2b, the weak BJH (Barrett–Joyner–Halenda) pore-size distribution peaks centered at 5 and 10 nm for the C_3N_4 NTs and C_3N_4 NTs (400 °C) samples are attributed to their poor mesoporous structures, which are constructed by accumulation of nanotubes structural units. The relatively strong pore-size distribution peaks in the range of 3–10 nm for the TiO_2 , $\text{TiO}_2@\text{C}_3\text{N}_4$ NTs, $\text{C-TiO}_2@\text{C}_3\text{N}_4$ NTs, and $\text{C/X-TiO}_2@\text{C}_3\text{N}_4$ NTs samples correspond to their rich mesoporous structures constructed by close accumulation of TiO_2 nanoparticles. The BET (Brunauer–Emmett–Teller) surface area of C_3N_4 NTs is larger than that of $\text{g-C}_3\text{N}_4$ because tubular nanostructure has both exposed internal and external geometrical surfaces with respect to the bulk layered structure. The similar BET surface areas of C_3N_4 NTs and C_3N_4 NTs (400 °C) samples indicate that C_3N_4 NTs obtained by one-step hydrothermal treatment strategy has a relatively stable microstructure. Interestingly, the BET surface areas of $\text{TiO}_2@\text{C}_3\text{N}_4$ NTs, $\text{C-TiO}_2@\text{C}_3\text{N}_4$ NTs, and $\text{C/X-TiO}_2@\text{C}_3\text{N}_4$ NTs are larger than that of TiO_2 and C_3N_4 NTs (400 °C). This result implies

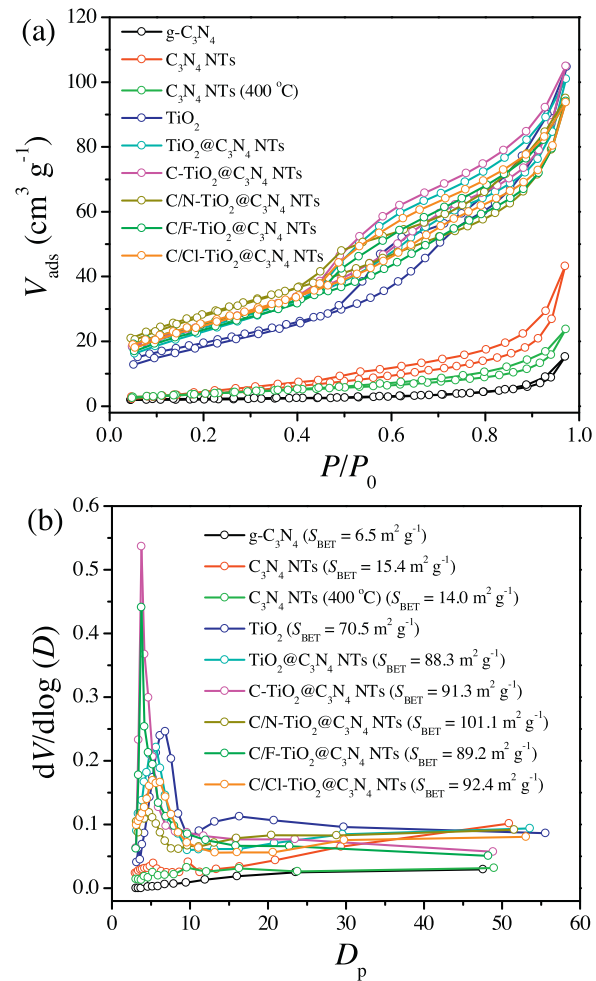


Fig. 2. Nitrogen gas sorption isotherms (a) and pore-size distribution curves (b) of as-prepared materials.

that the tubular nanostructure of C_3N_4 NTs precursor effectively inhibits the agglomeration of TiO_2 nanoparticles in the preparation process.

3.1.2. Compositional and structural information

The composition and structure of as-prepared materials are characterized by XRD, FTIR spectroscopy, and XPS. The phase structures of as-prepared materials are analyzed by XRD (Fig. 3). For the bulk layered $\text{g-C}_3\text{N}_4$, the strong (002) peak at 27.4° corresponds to an interlayer distance of $d = 0.33$ nm, whereas the (100) peak at 12.8° represents in-plane structural packing motif with a period of 0.675 nm. As for the C_3N_4 NTs, the intensity of (002) peak significantly decreases indicating that the layered structure units of bulk $\text{g-C}_3\text{N}_4$ has reduced and transformed morphologically into a tubular nanostructure after ultrasonic crashing and hydrothermal treatment. The as-prepared TiO_2 exhibits a pure anatase crystal phase with characteristic diffractions at 25.3° (101), 37.9° (004), 48.1° (200), 54.5° (105 + 211), and 62.6° (204) (JCPDS No. 21-1272). The XRD patterns of $\text{TiO}_2@\text{C}_3\text{N}_4$ NTs, $\text{C-TiO}_2@\text{C}_3\text{N}_4$ NTs, and $\text{C/X-TiO}_2@\text{C}_3\text{N}_4$ NTs show two-phase characteristic diffraction peaks of TiO_2 and C_3N_4 NTs, indicating the coexistence of TiO_2 and C_3N_4 NTs components in the composites.

FTIR spectra of as-prepared materials are shown in Fig. 4. For the $\text{g-C}_3\text{N}_4$, a series of peaks found in the range of 1700–1000 cm^{-1} is attributed to the stretching modes like C–N and C=N in the CN heterocycles. The sharp peak at 806.7 cm^{-1} is the typical bending

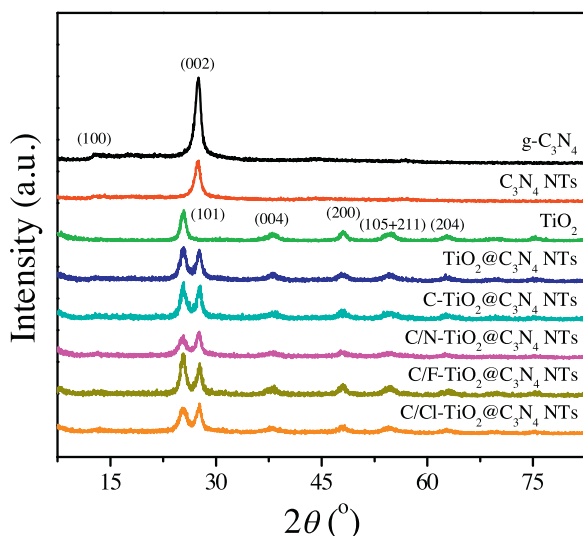


Fig. 3. XRD patterns of as-prepared materials.

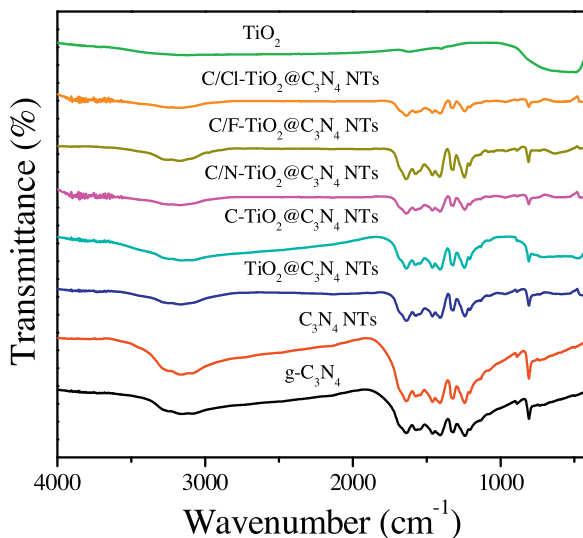


Fig. 4. FTIR spectra of as-prepared materials.

vibration of *s*-triazine units. The broad absorption peaks located in the range of 3400–2800 cm^{−1} originate from the stretching vibrational modes of primary (−NH₂) and secondary (=NH) amines. The FTIR spectrum of C₃N₄ NTs is similar to that of g-C₃N₄, indicating that C₃N₄ NTs keep the same chemical structure as g-C₃N₄ after ultrasonic crashing and hydrothermal treatment under acidic conditions. However, C₃N₄ NTs demonstrate a stronger FTIR mode compare with g-C₃N₄ owing to their more exposed surface functional groups. For the TiO₂@C₃N₄ NTs, C-TiO₂@C₃N₄ NTs, and C/X-TiO₂@C₃N₄ NTs samples, the FTIR mode corresponded to C₃N₄ NTs was weakened because of the surface functional groups on the C₃N₄ NTs were covered by TiO₂ nanoparticles. For the pure TiO₂, the broad peak in the range of 1000–420 cm^{−1} is attributed to the stretching modes of Ti—O—Ti covalent bonds. This broad peak can also be found in the FTIR spectra of TiO₂@C₃N₄ NTs, C-TiO₂@C₃N₄ NTs, and C/X-TiO₂@C₃N₄ NTs, indicating the coexistence of TiO₂ and C₃N₄ NTs components in the composites.

The existing interactions between the components in the as-prepared composites can be confirmed by high-resolution XPS analysis (Fig. 5). As shown in Fig. 5a, the C 1s peak centered at 284.6 eV is typically assigned to C—C or/and C=C, which originates from the adventitious reference carbon on the tested materials

surface. For the pure TiO₂, the C 1s peak centered at 288.4 eV is attributed to the C—OH groups, which originate from the organic species in the preparation process. For the C₃N₄ NTs, the C 1s peak centered at 287.6 eV originates from *sp*²C atoms bonded to N in an aromatic ring (N=C—(N)₂), whereas the C 1s peak centered at 288.4 eV is assigned to *sp*²C atoms in the aromatic ring attached to the secondary amine or hydroxyl (N=C(N)—NH, N=C(N)—OH). Our previous work has demonstrated that the —NH₂ groups within g-C₃N₄ has been substituted with —OH groups to form a N=C(N)—OH groups during the ultrasonic crashing and hydrothermal treatment under acidic conditions [39]. The C 1s peaks assigned to the C₃N₄ NTs shift to a higher binding energy direction after the formation of TiO₂@C₃N₄ NTs composite, indicating the existence of interactions between the interface of TiO₂ and C₃N₄ NTs. Based on this result it can be inferred that the surface N=C(N)—OH groups within C₃N₄ NTs interact with the surface Ti—OH groups within TiO₂ via N=C(N)—O—Ti covalent bonds in the TiO₂@C₃N₄ NTs composite. For the C/N-TiO₂@C₃N₄ NTs, the C 1s peaks of C₃N₄ NTs shift to a higher binding energy direction compare with TiO₂@C₃N₄ NTs, indicating that the formed lattice defect originated from co-doped nonmetallic elements impact the binding energy of TiO₂, and further impact the binding energy of C₃N₄ NTs. The results of N 1s XPS support the analysis of C 1s binding energy described above (Fig. 5b). For the C₃N₄ NTs, the peak centered at 398.0 eV is assigned to *sp*²-hybridized aromatic nitrogen atoms bonded to carbon atoms (C=N—C). The peak centered at 399.4 eV is related to either tertiary nitrogen ((C)₃—N) linking structural motifs C₆N₇ or amino groups carrying a hydrogen ((C)₂—NH) in connection with structural defects and incomplete condensation. There are no C—NH₂ structural units in the C₃N₄ NTs because of the missing —NH₂ groups in the course of ultrasonic crashing and hydrothermal treatment under acidic conditions. A weak peak at 400.5 eV corresponds to nitrogen atoms bonded to three carbon atoms in the aromatic cycles (N—(C)₃). The N 1s peaks of TiO₂@C₃N₄ NTs and C/N-TiO₂@C₃N₄ NTs gradually shift to a higher binding energy direction compare with C₃N₄ NTs, which can be attributed to the formation of N=C(N)—O—Ti covalent bonds between the interface of TiO₂ and C₃N₄ NTs and co-doped nonmetallic elements in TiO₂ indirectly impact the binding energy of C₃N₄ NTs. For the pure TiO₂, the determined binding energies of Ti 2p_{3/2} and Ti 2p_{1/2} are 458.0 and 463.8 eV, which is in good agreement with anatase TiO₂ (Fig. 5c). A slight shift of Ti 2p peaks was observed for the TiO₂@C₃N₄ NTs, indicating the existence of C—O—Ti covalent bonds between the interface of TiO₂ and C₃N₄ NTs. As for the C/N-TiO₂@C₃N₄ NTs, the shift of Ti 2p peaks is more obvious compare with TiO₂@C₃N₄ NTs owing to the formation of N—C—O—Ti covalent bond in TiO₂ component by nonmetallic elements co-doping. The XPS results of O 1s are consistent with that of Ti 2p (Fig. 5d). Pure TiO₂ shows three O 1s peaks with the binding energies of 529.2, 531.7, and 532.8 eV, which are attributed to the lattice-oxygen (Ti—O) and hydroxyl-oxygen (O—H) in anatase TiO₂ and carbon-oxygen (C—O) from the organic species in the preparation process. The O—H and C—O groups in C₃N₄ NTs can be attributed to the formation of N=C(N)—OH covalent bonds during the ultrasonic crashing and hydrothermal treatment under acidic conditions. A slight shift of O 1s peaks for the TiO₂@C₃N₄ NTs can be attributed to the existence of C—O—Ti covalent bonds between the interface of TiO₂ and C₃N₄ NTs. The obvious shift of O 1s peaks for the C/N-TiO₂@C₃N₄ NTs can be attributed to the formation of N—C—O—Ti covalent bond in TiO₂ component by nonmetallic elements co-doping. For the C/F-TiO₂@C₃N₄ NTs and C/Cl-TiO₂@C₃N₄ NTs, the XPS peaks of F 1s and Cl 2p centered at 683.8 and 198.0 eV directly prove the existence of F and Cl elements in the as-prepared composites (Fig. 5e and f).

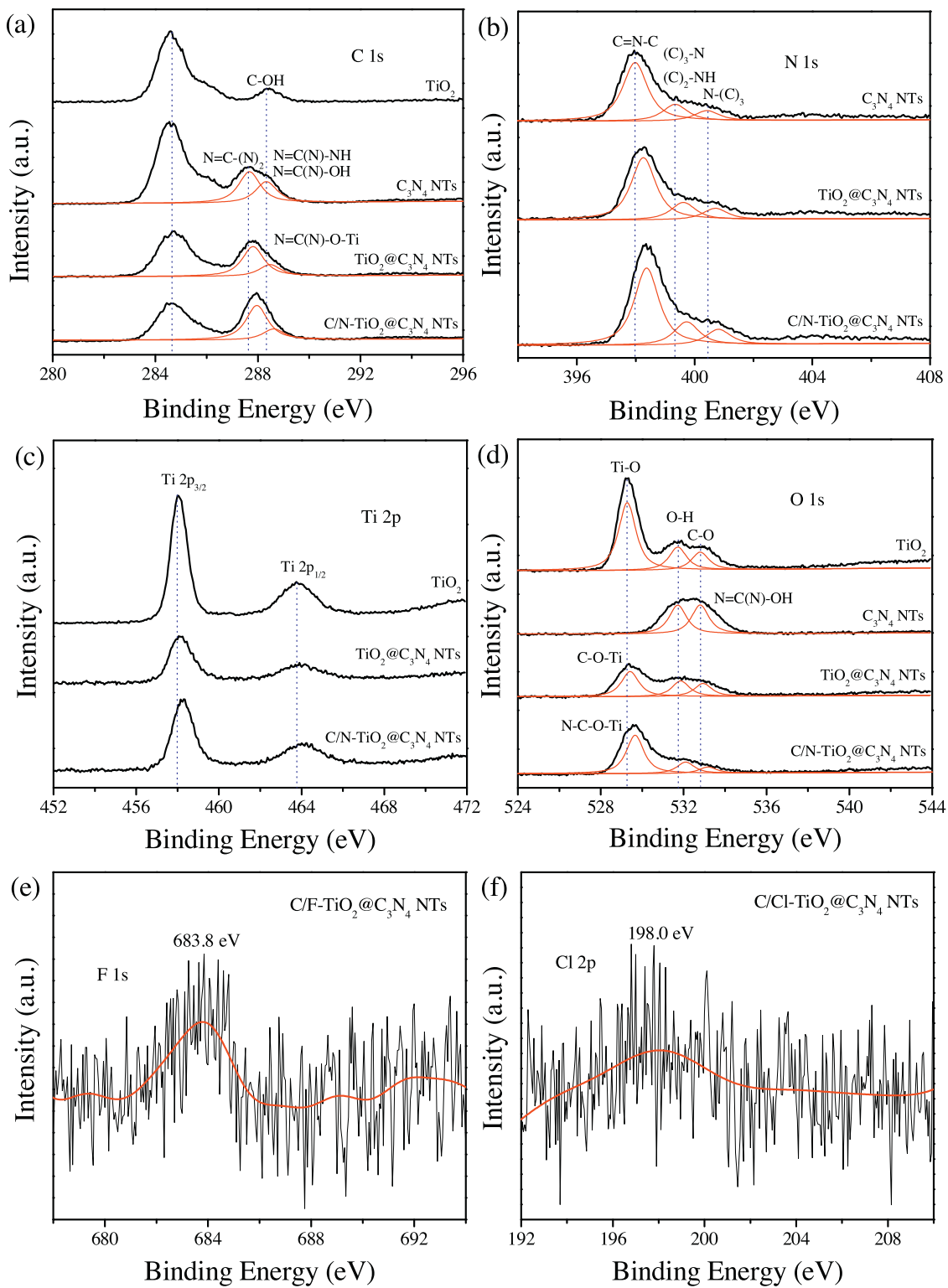
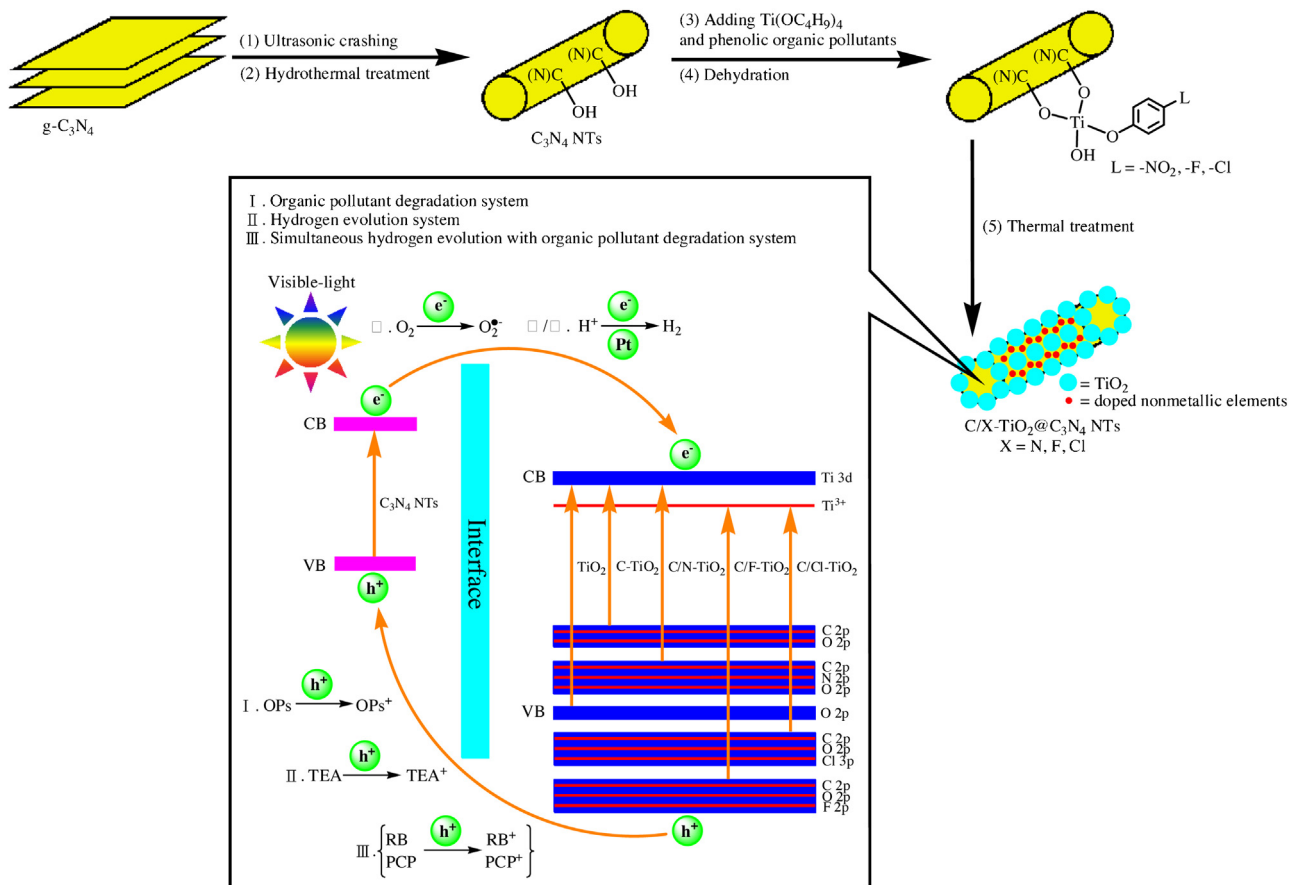


Fig. 5. High-resolution XPS of as-prepared materials in the C 1s (a), N 1s (b), Ti 2p (c), O 1s (d), F 2p (e), and Cl 2p (f) binding energy regions.

3.1.3. Optical and electronic properties

The light absorption properties of as-prepared materials were studied by UV-vis/DRS (Fig. 6). In order to exclude the interference of C₃N₄ NTs component, the light absorption properties of nonmetallic elements doped TiO₂ systems were firstly studied. As shown in Fig. 6a, pure TiO₂ shows a strong light response within the range of 200–400 nm, which can be attributed to the electron transition from the valence band (VB, O 2p) to the conduction band

(CB, Ti 3d). The weak light response of pure TiO₂ in the range of 400–800 nm is derived from the introduced carbon impurities in the preparation process. Compare with pure TiO₂, The enhanced light response throughout the tested wavelength for all the nonmetallic elements doped TiO₂ samples is attributed to the increased electronic transition efficiency from VB to CB, because new VB and CB were constructed in the nonmetallic elements doped TiO₂ composites (Scheme 1). Based on the conclusion that anatase TiO₂ is



Scheme 1. The designed route for fabrication of $\text{C}/\text{X}-\text{TiO}_2@\text{C}_3\text{N}_4$ NTs ($\text{X} = \text{N, F, Cl}$) composites and the separation and transportation of photoinduced charge carriers in the $\text{C}/\text{X}-\text{TiO}_2@\text{C}_3\text{N}_4$ NTs system under visible-light irradiation.

an indirect semiconductor, the band gap energies of as-prepared nonmetallic elements doped TiO_2 composites can be calculated through the following equation:

$$(\alpha h\nu)^{1/2} = A(h\nu - E_g)$$

where α represents the absorption coefficient, h is Plank's constant, ν is the light frequency, and A is a constant. From the plot of $(\alpha h\nu)^{1/2}$ versus photon energy ($h\nu$) it can be estimated that the band gap energies of TiO_2 , C-TiO_2 , C/N-TiO_2 , C/F-TiO_2 , and C/Cl-TiO_2 are 2.88, 2.45, 2.73, 2.95, and 2.91 eV, respectively (Fig. 6b). The lower band gap energy of as-prepared TiO_2 compare with traditional P25 photocatalyst (3.2 eV) can be attributed to the introduction of carbon impurities in the preparation process. As shown in Fig. 6c, $\text{g-C}_3\text{N}_4$ shows a typical semiconductor absorption within the region of 200–450 nm, which originates from the electron transition from VB populated by N 2p orbit to CB formed by C 2p orbit. The light absorption ability of C_3N_4 NTs was increased compared with that of $\text{g-C}_3\text{N}_4$ owing to their nano-size effect, because tubular nanostructure is more beneficial than their corresponding bulk structure for multiple reflections of incident light. For the $\text{TiO}_2@\text{C}_3\text{N}_4$ NTs, a new light absorption signal exist in the range of 450–800 nm with respect to pure TiO_2 and C_3N_4 NTs, implying the existence of electron transition between the TiO_2 and C_3N_4 NTs components. For the $\text{C-TiO}_2@\text{C}_3\text{N}_4$ NTs and $\text{C}/\text{X}-\text{TiO}_2@\text{C}_3\text{N}_4$ NTs samples, the stronger light absorption abilities compare with $\text{TiO}_2@\text{C}_3\text{N}_4$ NTs throughout the tested wavelength are attributed to the nonmetallic elements doping in TiO_2 component that have been described in Fig. 6a.

The conduction band potential (E_{CB}) of as-prepared nonmetallic elements doped TiO_2 was determined by their corresponding

Mott–Schottky plots. As shown in Fig. 7, the flat-band potential (V_{fb}) obtained by extrapolation of the Mott–Schottky plots is roughly -0.86 V for TiO_2 , C-TiO_2 , and C/N-TiO_2 samples and -0.73 V for C/F-TiO_2 and C/Cl-TiO_2 samples versus SCE as pH 7. After correction by adding $+0.24$ V, the E_{CB} of TiO_2 , C-TiO_2 , and C/N-TiO_2 is about -0.62 V and the E_{CB} of C/F-TiO_2 and C/Cl-TiO_2 is about -0.49 V. Based on the above UV-vis/DRS and Mott–Schottky plots results, the energy band structure diagram of as-prepared materials is shown in Scheme 1.

The photocatalytic quantum efficiencies of as-prepared materials were studied by PL measurements. As shown in Fig. 8, $\text{g-C}_3\text{N}_4$ exhibits a broad fluorescence emission peak in the range of 400–600 nm with an excitation wavelength of 330 nm and an operating voltage of 400 V. This finding suggests that photoinduced e^- – h^+ pairs are generated and recombined within the $\text{g-C}_3\text{N}_4$. Compare with $\text{g-C}_3\text{N}_4$, the decreased PL intensity of C_3N_4 NTs indicates that the efficient separation and transportation of photogenerated carriers are realized after the formation of tubular nanostructure. For the $\text{TiO}_2@\text{C}_3\text{N}_4$ NTs, the obviously decreased PL intensity compared with C_3N_4 NTs can be attributed to the efficient transportation of photogenerated carriers between the interface of TiO_2 and C_3N_4 NTs. Compare with $\text{TiO}_2@\text{C}_3\text{N}_4$ NTs, the PL intensities of $\text{C-TiO}_2@\text{C}_3\text{N}_4$ NTs and $\text{C}/\text{X}-\text{TiO}_2@\text{C}_3\text{N}_4$ NTs are further decreased, because doped nonmetallic elements increase the electronic transition efficiency of TiO_2 component. Based on the above discussion of the characterization results, the designed route for fabrication of $\text{C}/\text{X}-\text{TiO}_2@\text{C}_3\text{N}_4$ NTs and the separation and transportation of photoinduced charge carriers in the $\text{C}/\text{X}-\text{TiO}_2@\text{C}_3\text{N}_4$ NTs system under visible-light irradiation are shown in Scheme 1.

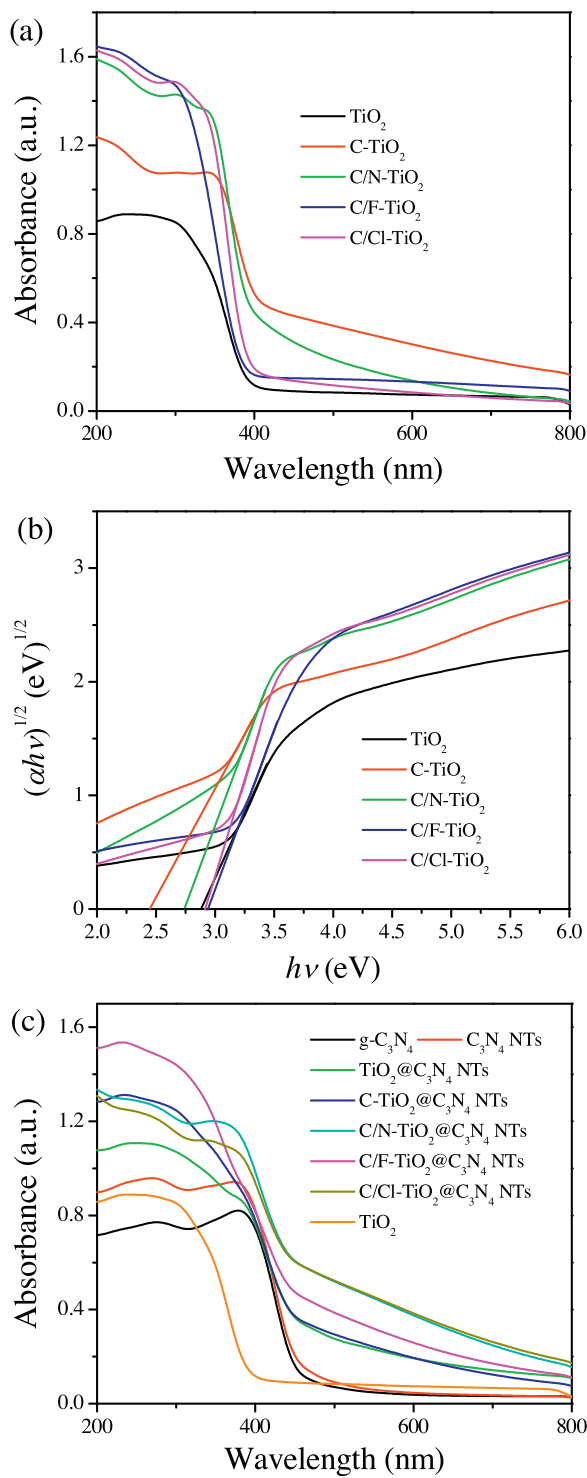


Fig. 6. UV-vis/DRS of as-prepared materials.

3.2. Photocatalytic tests

3.2.1. Photocatalytic degradation of aqueous MO and PCP

The photocatalytic degradation tests were conducted in an aqueous solution containing oxygen molecules from dissolved air. As shown in Fig. 9a and b, the results of direct photodegradation experiment indicate that changes of MO and PCP concentrations in the reaction system are negligible under visible-light irradiation for 4 and 6 h, respectively. The adsorption test results show that the adsorption-desorption equilibrium had been reached prior to

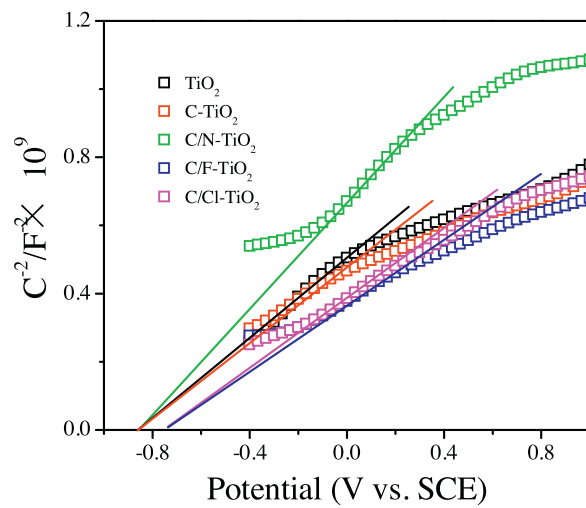


Fig. 7. Electrochemical Mott-Schottky plots of as-prepared materials at 1000 Hz frequency in $0.5 \text{ mol L}^{-1} \text{ Na}_2\text{SO}_4$ aqueous solution.

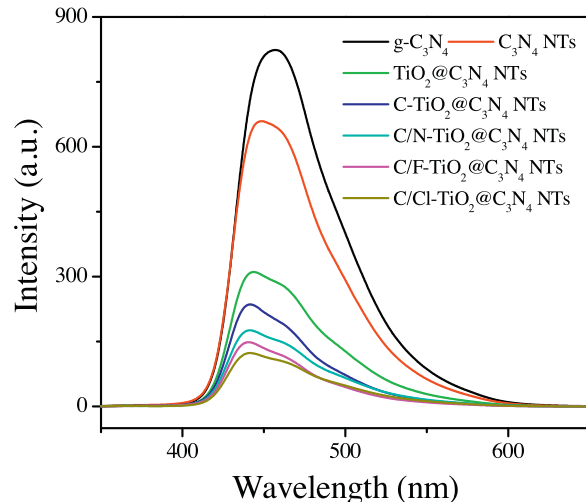


Fig. 8. PL spectra of as-prepared materials.

Xe lamp irradiation. For the aqueous MO degradation, the photocatalytic activities of as-prepared materials followed the order of $\text{C/F-TiO}_2@\text{C}_3\text{N}_4$ NTs $>$ $\text{C/Cl-TiO}_2@\text{C}_3\text{N}_4$ NTs $>$ $\text{C/N-TiO}_2@\text{C}_3\text{N}_4$ NTs $>$ $\text{C-TiO}_2@\text{C}_3\text{N}_4$ NTs \geq $\text{TiO}_2@\text{C}_3\text{N}_4$ NTs $>$ $\text{TiO}_2@g-\text{C}_3\text{N}_4$ $>$ C_3N_4 NTs (400 °C) $>$ C_3N_4 NTs $>$ TiO_2 $>$ $g-\text{C}_3\text{N}_4$. For the aqueous PCP degradation, the photocatalytic activities of as-prepared materials followed the order of $\text{C/Cl-TiO}_2@\text{C}_3\text{N}_4$ NTs $>$ $\text{C/F-TiO}_2@\text{C}_3\text{N}_4$ NTs $>$ $\text{C/N-TiO}_2@\text{C}_3\text{N}_4$ NTs $>$ $\text{C-TiO}_2@\text{C}_3\text{N}_4$ NTs \geq $\text{TiO}_2@\text{C}_3\text{N}_4$ NTs $>$ $\text{TiO}_2@g-\text{C}_3\text{N}_4$ $>$ TiO_2 $>$ C_3N_4 NTs (400 °C) $>$ C_3N_4 NTs $>$ $g-\text{C}_3\text{N}_4$. Compare with C_3N_4 NTs, the slightly increased photocatalytic activity of C_3N_4 NTs (400 °C) can be attributed to the thermal effect of secondary calcination [33]. The photocatalytic activities of C_3N_4 NTs and $\text{TiO}_2@\text{C}_3\text{N}_4$ NTs are higher than that of $g-\text{C}_3\text{N}_4$ and $\text{TiO}_2@g-\text{C}_3\text{N}_4$ for both of MO and PCP degradation owing to the constructed tubular nanostructures. For the pure TiO_2 , the photocatalytic activity is lower than C_3N_4 NTs toward MO degradation but higher than C_3N_4 NTs for the PCP degradation. This result can be attributed to the different affinity between the photocatalyst and organic pollutant. Specifically, the negatively charged surface $\text{Ti}-\text{OH}$ in TiO_2 is exclusive to the anionic dyes MO but attractive to the PCP owing to the existence of hydrogen bonds between $\text{Ti}-\text{OH}$ and PCP molecule. In addition, the existence of visible-light photocatalytic activity for the pure TiO_2

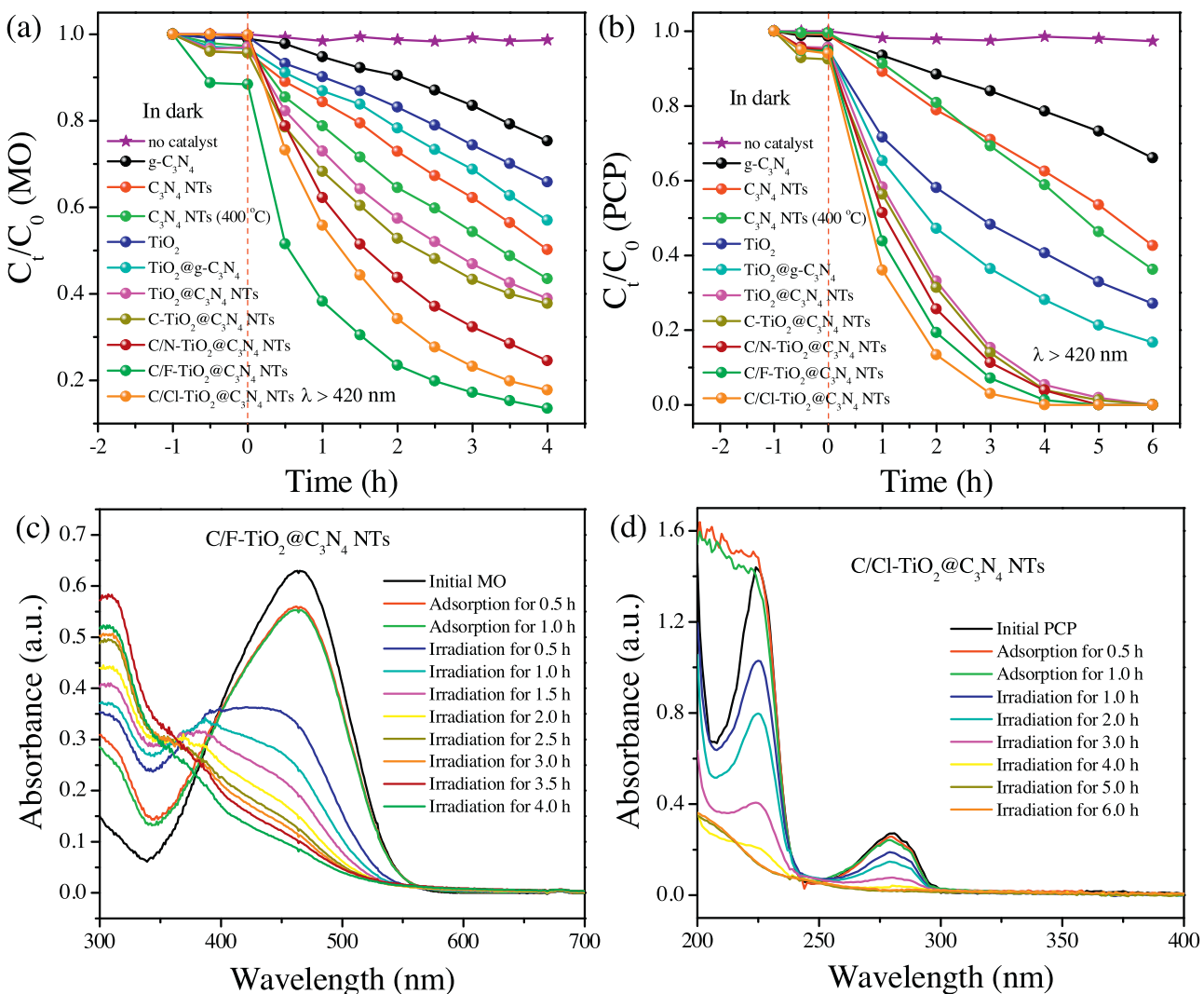


Fig. 9. Adsorption properties and visible-light photocatalytic degradation activities of as-prepared materials toward aqueous MO (a) and PCP (b); UV-vis adsorption spectra of MO (c) and PCP (d) solution as a function of irradiation time during the photocatalytic degradation process over C/F-TiO₂@C₃N₄ NTs and C/Cl-TiO₂@C₃N₄ NTs photocatalysts.

can be attributed to the formed impurity level in the preparation process. The visible-light photocatalytic activity of $\text{TiO}_2@C_3\text{N}_4$ NTs enhance significantly compared with that of TiO_2 and C_3N_4 NTs because of the efficient transportation of photogenerated carriers between the interface of TiO_2 and C_3N_4 NTs. For the $\text{C-TiO}_2@C_3\text{N}_4$ NTs and $\text{C/X-TiO}_2@C_3\text{N}_4$ NTs samples, the further enhanced visible-light photocatalytic activity compared with $\text{TiO}_2@C_3\text{N}_4$ NTs can be attributed to the formed impurity levels enhance the electronic transition efficiency of TiO_2 component. The photocatalytic activity should be increased with increasing the quantum efficiency of the photocatalyst and the appropriate band gap structure of TiO_2 component is advantageous for the transportation of photogenerated carriers between the interface of TiO_2 and C_3N_4 NTs. Therefore, both the photocatalytic activity and quantum efficiency should follow the order of $\text{C/Cl-TiO}_2@C_3\text{N}_4$ NTs > $\text{C/F-TiO}_2@C_3\text{N}_4$ NTs > $\text{C/N-TiO}_2@C_3\text{N}_4$ NTs > $\text{C-TiO}_2@C_3\text{N}_4$ NTs. However, $\text{C/F-TiO}_2@C_3\text{N}_4$ NTs exhibit higher photocatalytic activity than $\text{C/Cl-TiO}_2@C_3\text{N}_4$ NTs toward MO degradation, because the strong electron-withdrawing capacity of $-F$ groups lead to the strong adsorption capacity of $\text{C/F-TiO}_2@C_3\text{N}_4$ NTs to MO molecules.

Fig. 9c and d shows the variations of the characteristic absorption of MO (at 464 nm) and PCP (at 277 nm) under visible-light irradiation by using $\text{C/F-TiO}_2@C_3\text{N}_4$ NTs and $\text{C/Cl-TiO}_2@C_3\text{N}_4$ NTs

as the photocatalyst, respectively. The characteristic absorptions of MO and PCP gradually reduce with prolonging the irradiation time, and the characteristic absorptions of MO and PCP is hardly observed after 4 and 6 h visible-light irradiation. These results are consistent with those shown in Fig. 9a and b.

The mineralization of aqueous MO and PCP was evaluated by monitoring the changes in total organic carbon (TOC) in the reaction system. $\text{C/F-TiO}_2@C_3\text{N}_4$ NTs and $\text{C/Cl-TiO}_2@C_3\text{N}_4$ NTs were selected as the representative photocatalysts, and the results are shown in Fig. 10a. TOC of MO and PCP are degraded by 52.5% and 74.7%, respectively, after exposure to visible-light irradiation for 18 h, indicating that the produced organic intermediates continue to decompose into inorganic species. MO mineralization rate is slower than PCP under similar conditions because of the relatively stable chemical structure of MO molecule.

$\text{C/Cl-TiO}_2@C_3\text{N}_4$ NTs was chosen to evaluate the recyclability of the catalyst. The above PCP degradation reaction was repeated for five times. After the first catalytic run, the catalyst was recovered by centrifugation, and then it was washed by water at room temperature. The recovered catalyst was used for the subsequent catalytic runs under the same experimental conditions. The result shows that the tested catalysts exhibit considerably high stability, and they can maintain a similar level of reactivity after five catalytic cycles (Fig. 10b).

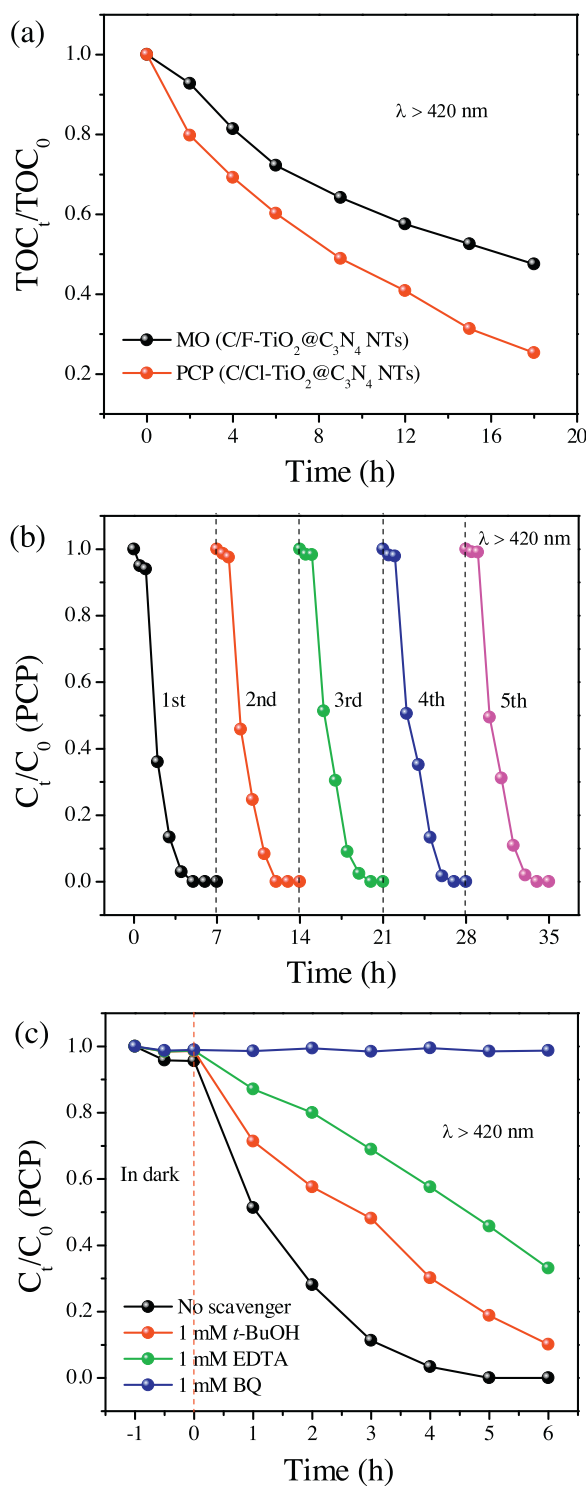


Fig. 10. Evolution of TOC during the course of photocatalytic degradation of aqueous MO and PCP over $\text{C}/\text{F}-\text{TiO}_2@\text{C}_3\text{N}_4$ NTs and $\text{C}/\text{Cl}-\text{TiO}_2@\text{C}_3\text{N}_4$ NTs photocatalysts (a); recycling experiments of photocatalytic degradation of aqueous PCP over $\text{C}/\text{Cl}-\text{TiO}_2@\text{C}_3\text{N}_4$ NTs photocatalyst (b); influence of various scavengers on the visible-light photocatalytic activity of $\text{C}-\text{TiO}_2@\text{C}_3\text{N}_4$ NTs photocatalyst toward PCP degradation (c).

In order to clarify what kind of active species played a key role during the photocatalytic degradation, the active species masking experiments were carried out by using $\text{C}-\text{TiO}_2@\text{C}_3\text{N}_4$ NTs as a representative photocatalyst and PCP as a target pollutant. In this study, *tert*-butyl alcohol ($t\text{-BuOH}$), ethylenediaminetetraacetic acid (EDTA), and 1,4-benzoquinone (BQ) are used as the hydroxyl radical

($\cdot\text{OH}$) scavenger, hole (h^+) scavenger, and superoxide radical ($\cdot\text{O}_2^-$) scavenger, respectively. As shown in Fig. 10c, the degradation rate of PCP is inhibited somewhat compared with scavenger-free photocatalytic system after adding $t\text{-BuOH}$ (1 mmol L^{-1}). However, the degradation rate of PCP is decelerated obviously in the presence of EDTA (1 mmol L^{-1}). Finally, the degradation of PCP is inhibited completely after adding BQ (1 mmol L^{-1}). The above results indicate that $\cdot\text{O}_2^-$ is the principal active species, h^+ is the secondary active species, and $\cdot\text{OH}$ is the unimportant active species in the course of photocatalytic degradation.

3.2.2. Hydrogen evolution from water-splitting by using TEA or organic pollutant as an electron donor

TEA is commonly used as an electron donor in the traditional photocatalytic hydrogen evolution system. Therefore, the photocatalytic activities of $\text{C}-\text{TiO}_2@\text{C}_3\text{N}_4$ NTs and $\text{C}/\text{X}-\text{TiO}_2@\text{C}_3\text{N}_4$ NTs for hydrogen evolution from water-splitting were evaluated in a 20 vol% TEA aqueous solution under $\lambda > 420 \text{ nm}$ visible-light irradiation for 6 h in the presence of 3 wt% Pt co-catalyst. As shown in Fig. 11a, all the tested samples show the excellent hydrogen evolution activity followed the order of $\text{C}/\text{N}-\text{TiO}_2@\text{C}_3\text{N}_4$ NTs > $\text{C}/\text{Cl}-\text{TiO}_2@\text{C}_3\text{N}_4$ NTs > $\text{C}/\text{F}-\text{TiO}_2@\text{C}_3\text{N}_4$ NTs > $\text{C}-\text{TiO}_2@\text{C}_3\text{N}_4$ NTs. The similar electronic structure characteristics of $-\text{N}$ groups in $\text{C}/\text{N}-\text{TiO}_2@\text{C}_3\text{N}_4$ NTs and N atoms in TEA make the relatively strong affinity exist between $\text{C}/\text{N}-\text{TiO}_2@\text{C}_3\text{N}_4$ NTs and TEA molecules. Therefore, $\text{C}/\text{N}-\text{TiO}_2@\text{C}_3\text{N}_4$ NTs exhibit higher photocatalytic hydrogen evolution activity than $\text{C}/\text{Cl}-\text{TiO}_2@\text{C}_3\text{N}_4$ NTs.

Based on our previous work, the simultaneous hydrogen evolution with organic pollutant degradation system was further studied by using $\text{C}/\text{N}-\text{TiO}_2@\text{C}_3\text{N}_4$ NTs as the photocatalyst, which exhibit the highest photocatalytic activity in conventional hydrogen evolution system. As shown in Fig. 11b, the hydrogen yield decrease significantly in H_2O , TEA, PCP/ H_2O , and RB/ H_2O systems, and the degradation efficiency of PCP significantly decrease at the same time compared with conventional photocatalytic degradation system. We try to improve the hydrogen yield by increasing the concentration of organic pollutant or prolonging the irradiation time in the simultaneous hydrogen evolution with organic pollutant degradation system. Unfortunately, the hydrogen yield only slightly increases with increasing the concentration of organic pollutant and prolonging the irradiation time (Fig. 11c and d). In addition, the degradation efficiency of RB decreases with increasing the concentration of RB and increases with prolonging the irradiation time.

3.2.3. Discussion of reaction mechanism in different photocatalytic systems

Based on the above photocatalytic activity results, the reaction mechanism in different photocatalytic systems are discussed below. Firstly, there are two questions must be clear that both photocatalytic degradation and hydrogen evolution reaction belong to the redox processes and photocatalyst act as an electron transfer medium in the redox process. Specifically, oxygen act as an oxidizing agent and organic pollutant act as a reducing agent in a conventional photocatalytic degradation system, moreover, water act as an oxidizing agent and electron donor act as a reducing agent in a conventional photocatalytic hydrogen evolution system. The redox reaction can be successfully carried out owing to the simultaneous presence of oxidizing and reducing agent in a conventional photocatalytic system. Therefore, the effect of photocatalytic reaction is mainly influenced by the properties of the photocatalyst. The constructed tubular nanostructure, enlarged BET surface area, perfect phase structure, improved light absorption capacity, and increased quantum efficiency play positive roles to enhance the activity of the photocatalyst. Therefore, the as-prepared $\text{C}/\text{X}-\text{TiO}_2@\text{C}_3\text{N}_4$ NTs composites exhibit excellent

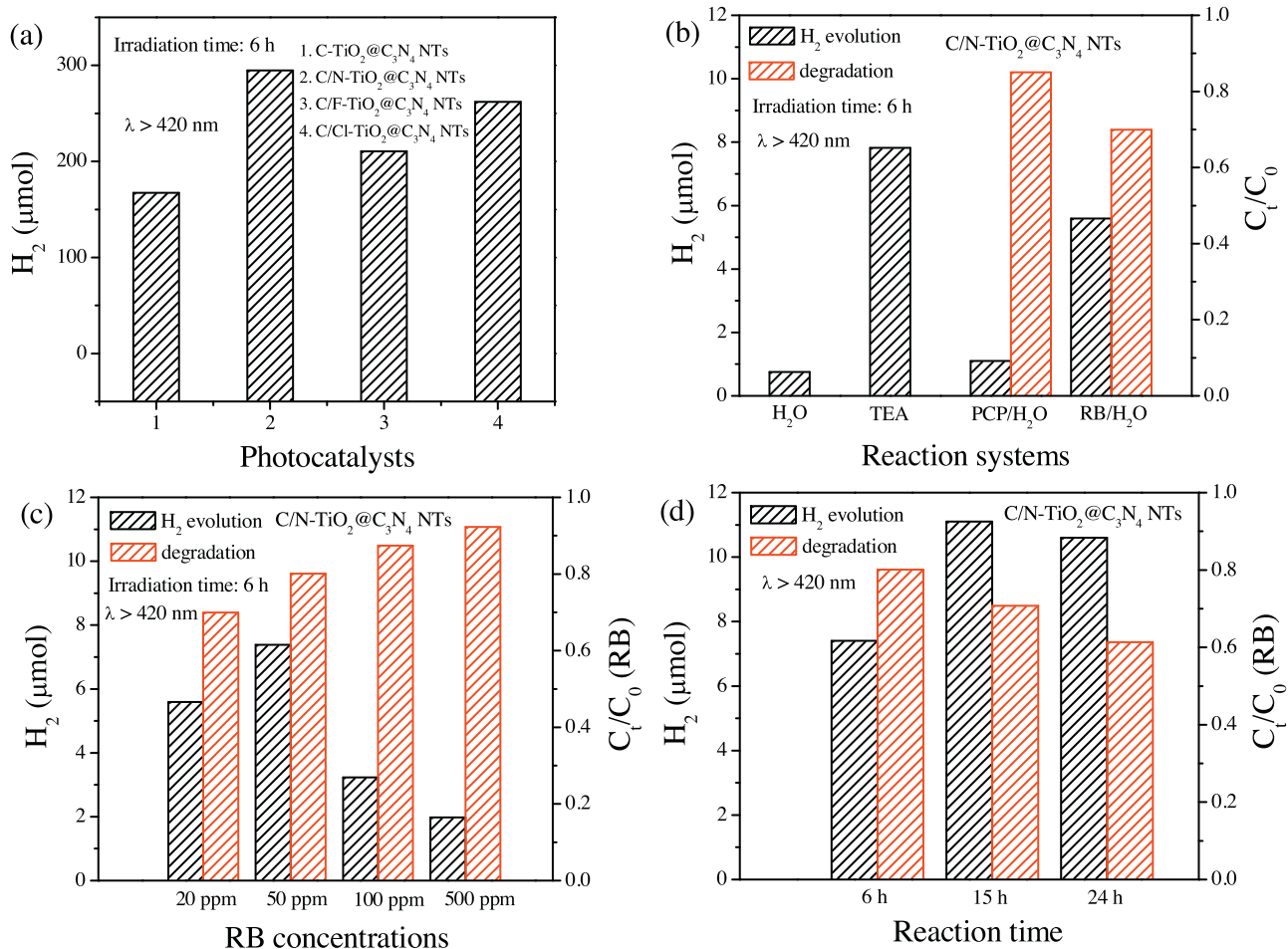


Fig. 11. Hydrogen evolution from water-splitting over as-prepared photocatalysts by using TEA as an electron donor (a); simultaneous hydrogen evolution with organic pollutant degradation by using $\text{C}/\text{N-TiO}_2@\text{C}_3\text{N}_4$ NTs as a photocatalyst: different reaction systems (b), RB concentrations (c), and reaction time (d).

photocatalytic activity toward both degradation and hydrogen evolution reaction in the conventional photocatalytic system. In the active species masking experiments, the dissolved oxygen was consumed because of the addition of BQ in the photocatalytic degradation system, therefore, the redox reaction between oxygen and organic pollutant is inhibited completely. In addition, the electron transfer effect of photocatalyst is weakened because the added EDTA consumed the photogenerated h^+ . Therefore, the redox reaction between the oxygen and organic pollutant is also inhibited significantly. The unobvious $\cdot\text{OH}$ masking effect of $t\text{-BuOH}$ can be understood that $t\text{-BuOH}$ or organic pollutant reacts with dissolved oxygen are competitive. In the single-component (pure H_2O or TEA) hydrogen evolution system, the redox reaction only carries out within the H_2O or TEA molecule due to the lack of reducing agent (TEA) or oxidizing agent (H_2O), therefore, the hydrogen yield is low. For the PCP/ H_2O and RB/ H_2O simultaneous hydrogen evolution with organic pollutant degradation system, the redox reaction between organic pollutants and H_2O hardly carries out due to the poor electron-donating ability of organic pollutants. Therefore, both the hydrogen yield and degradation efficiency are significantly decreased compared with conventional photocatalytic degradation and hydrogen evolution systems. The increased organic pollutant (reducing agent) concentration is advantageous for the proceeding of redox reaction, but excessively high concentration of organic pollutant is not conducive to carry out the redox reaction due to the relatively strong hydrogen bonding and electrostatic interaction between the organic pollutant molecules. Therefore, the condition of appropriate RB concentration (50 ppm) shows the highest hydro-

gen yield in the RB/ H_2O simultaneous hydrogen evolution with organic pollutant degradation system. In addition, the prolonged irradiation time make the redox reaction between RB and H_2O continuously carry out. Therefore, both hydrogen yield and degradation efficiency can be further improved. However, excessively long irradiation time make the hydrogen yield declined slightly due to the generated oxidizing species react with hydrogen in the process of RB degradation.

4. Conclusions

A series of $\text{C}/\text{X-TiO}_2@\text{C}_3\text{N}_4$ NTs ($\text{X}=\text{N, F, Cl}$) composites was successfully prepared by a simple sol-gel-pyrolysis process using phenolic organic pollutants, titanium butoxide, and carbon nitride nanotubes as precursors. The showing efficient activity of as-prepared $\text{C}/\text{X-TiO}_2@\text{C}_3\text{N}_4$ NTs under visible-light irradiation in conventional photocatalytic degradation and hydrogen evolution system can be attributed to their constructed tubular nanostructure, enlarged BET surface area, perfect phase structure, improved light absorption capacity, and increased quantum efficiency. The redox reaction between organic pollutants and H_2O hardly carried out due to the poor electron-donating ability of organic pollutants in the simultaneous hydrogen evolution with organic pollutant degradation system. As a result, both hydrogen yield and degradation efficiency are significantly decreased compared with conventional photocatalytic degradation and hydrogen evolution systems.

Acknowledgements

This work was financially supported by the National Natural Science Foundation of China (51238001, 51568049, 51208248, 51278092, 51238002, 51272099, 21366024); Science and Technology Major Bidding Project of Jiangxi Province, China (No. Gan Ke Fa Ji Zi [2010] 217); Youth Science Foundation of Jiangxi Province, China (20114BAB213015); Technology Project of Jiangxi Provincial Department of Education, China (GJJ12456, GJJ14515).

References

- [1] K.F. Chasib, J. Chem. Eng. Data 58 (2013) 1549–1564.
- [2] S. Mondal, R. Mukherjee, S. De, 2015, Ind. Eng. Chem. Res. 54 (2015) 514–521.
- [3] K. Baransi, Y. Dubowski, I. Sabbah, Water Res. 46 (2012) 789–798.
- [4] M.R. Gonçalves, J.C. Costa, I.P. Marques, M.M. Alves, Water Res. 46 (2012) 1684–1692.
- [5] S.S. Kontos, P.G. Koutsoukos, C.A. Paraskeva, Chem. Eng. J. 251 (2014) 319–328.
- [6] M. Zhang, L. Zhi, H. Li, H. Long, W. Zhao, Chem. Eng. J. 229 (2013) 99–104.
- [7] S. Kim, W. Choi, J. Phys. Chem. B 109 (2005) 5143–5149.
- [8] Y. Zheng, L. Lin, B. Wang, X. Wang, Angew. Chem. Int. Ed. 54 (2015) 12868–12884.
- [9] M.K. Bhunia, K. Yamauchi, K. Takanabe, Angew. Chem. Int. Ed. 53 (2014) 11001–11005.
- [10] Y.S. Jun, J. Park, S.U. Lee, A. Thomas, W.H. Hong, G.D. Stucky, Angew. Chem. Int. Ed. 52 (2013) 11083–11087.
- [11] A.C. Pradhan, B. Nanda, K.M. Parida, Mira Das, Dalton Trans. 42 (2013) 558–566.
- [12] Y. Wu, H. Luo, X. Jiang, H. Wang, J. Geng, RSC Adv. 5 (2015) 4905–4908.
- [13] R. Vinu, S. Polisetti, G. Madras, Chem. Eng. J. 165 (2010) 784–797.
- [14] K. Bourikas, C. Kordulis, A. Lycourghiotis, Chem. Rev. 114 (2014) 9754–9823.
- [15] K. Schwinghammer, M.B. Mesch, V. Duppel, C. Ziegler, J. Senker, B.V. Lotsch, J. Am. Chem. Soc. 136 (2014) 1730–1733.
- [16] H. Liu, J.B. Joo, M. Dahl, L. Fu, Z. Zeng, Y. Yin, Energy Environ. Sci. 8 (2015) 286–296.
- [17] F. He, G. Chen, Y. Zhou, Y. Yu, Y. Zheng, S. Hao, Chem. Commun. 51 (2015) 16244–16246.
- [18] M. Raula, G.G. Or, M. Saganovich, O. Zeiri, Y. Wang, M.R. Chierotti, R. Gobetto, I.A. Weinstock, Angew. Chem. Int. Ed. 54 (2015) 12416–12421.
- [19] Y. Kang, Y. Yang, L. Yin, X. Kang, G. Liu, H. Cheng, Adv. Mater. 27 (2015) 4572–4574.
- [20] K. Li, S. Gao, Q. Wang, H. Xu, Z. Wang, B. Huang, Y. Dai, J. Lu, ACS Appl. Mater. Interfaces 7 (2015) 9023–9030.
- [21] Y. Zang, L. Li, Y. Xu, Y. Zuo, G. Li, J. Mater. Chem. A 2 (2014) 15774–15780.
- [22] L. Zhang, D. Jing, X. She, H. Liu, D. Yang, Y. Lu, J. Li, Z. Zheng, L. Guo, J. Mater. Chem. A 2 (2014) 2071–2078.
- [23] W. Ma, D. Han, M. Zhou, H. Sun, L. Wang, X. Dong, L. Niu, Chem. Sci. 5 (2014) 3946–3951.
- [24] J. Xu, G. Wang, J. Fan, B. Liu, S. Cao, J. Yu, J. Power Sources 274 (2015) 77–84.
- [25] Z. Huang, Q. Sun, K. Lv, Z. Zhang, M. Li, B. Li, Appl. Catal. B: Environ. 164 (2015) 420–427.
- [26] V. Trevisan, A. Olivo, F. Pinna, M. Signoretto, F. Vindigni, G. Cerrato, C.L. Bianchi, Appl. Catal. B: Environ. 160–161 (2014) 152–160.
- [27] J. Zhang, Y. Chen, X. Wang, Energy Environ. Sci. 8 (2015) 3092–3108.
- [28] Z. Lin, X. Wang, Angew. Chem. Int. Ed. 52 (2013) 1735–1738.
- [29] D.H. Wang, L. Jia, X.L. Wu, L.Q. Lu, A.W. Xu, Nanoscale 4 (2012) 576–584.
- [30] G. Zhang, M. Zhang, X. Ye, X. Qiu, S. Lin, X. Wang, Adv. Mater. 26 (2014) 805–809.
- [31] D. Zheng, C. Pang, Xincheng Wang, Chem. Commun. 51 (2015) 17467–17470.
- [32] D. Zheng, C. Pang, Y. Liu, X. Wang, Chem. Commun. 51 (2015) 9706–9709.
- [33] D. Zheng, C. Huang, X. Wang, Nanoscale 7 (2015) 465–470.
- [34] M. Zhang, Z. Luo, M. Zhou, C. Huang, X. Wang, Sci. China Mater. 58 (2015) 867–876.
- [35] X. Chen, C. Burda, J. Am. Chem. Soc. 130 (2008) 5018–5019.
- [36] S. Yang, Y. Gong, J. Zhang, L. Zhan, L. Ma, Z. Fang, R. Vajtai, X. Wang, P.M. Ajayan, Adv. Mater. 25 (2013) 2452–2456.
- [37] C. Huang, C. Chen, M. Zhang, L. Lin, X. Ye, S. Lin, M. Antonietti, X. Wang, Nat. Commun. 6 (2015) 7698 (1–7).
- [38] K. Li, J. Xiong, T. Chen, L. Yan, Y. Dai, D. Song, Y. Lv, Z. Zeng, J. Hazard. Mater. 250–251 (2013) 19–1928.
- [39] K. Li, L. Yan, Z. Zeng, S. Luo, X. Luo, X. Liu, H. Guo, Y. Guo, Appl. Catal. B: Environ. 156–157 (2014) 141–152.
- [40] Z. Zeng, K. Li, L. Yan, Y. Dai, H. Guo, M. Huo, Y. Guo, RSC Adv. 4 (2014) 59513–59518.
- [41] J. Kim, D. Monllor-Satoca, W. Choi, Energy Environ. Sci. 5 (2012) 7647–7656.
- [42] K. Li, Z. Zeng, L. Yan, S. Luo, X. Luo, M. Huo, Y. Guo, Appl. Catal. B: Environ. 165 (2015) 428–437.